Nanoscale

PAPER

View Article Online
View Journal | View Issue

Cite this: *Nanoscale*, 2023, **15**, 13402

Origin and regulation of triaxial magnetic anisotropy in the ferromagnetic semiconductor CrSBr monolayer†

Bing Wang, Yaxuan Wu, Yihang Bai, Puyuan Shi, Guangbiao Zhang,* Yungeng Zhang* and Chang Liu*

Received 30th May 2023,
Accepted 20th July 2023

DOI: 10.1039/d3nr02518g

rsc.li/nanoscale

Magnetic anisotropy plays a vital role in stabilizing the long-range magnetic order of two-dimensional ferromagnetic systems. In this work, using the first-principles method, we systematically explored the triaxial magnetic anisotropic properties of a ferromagnetic semiconductor CrSBr monolayer, which is recently exfoliated from its bulk. Further analysis shows that the triaxial magnetic anisotropic properties originate from the coexistence of the magnetic dipole–dipole interaction (shape anisotropy) and the spin–orbit coupling interaction (magnetocrystalline anisotropy). Interestingly, the shape anisotropy, which has been neglected in most previous works, dominates over the magnetocrystalline anisotropy. Besides, the experimental Curie temperature of the CrSBr monolayer is well reproduced using Monte Carlo simulations. What is more, the easy magnetic axes and ferromagnetism in the CrSBr monolayer can be manipulated by strains and are relatively more susceptible to the uniaxial strain in the *x* direction. Our study not only explains the mechanism of triaxial magnetic anisotropy of the CrSBr monolayer, but also sheds light on how to tune the magnetic anisotropy and Curie temperature in ferromagnetic monolayers.

Introduction

Spintronic devices have attracted widespread attention because of their advantages of faster processing speed, ultra-low heat dissipation, denser storage density, lower power consumption, and non-volatility.[1–5] With the need for the miniaturization of spintronic devices, intrinsic two-dimensional (2D) ferromagnetic semiconductor (FMS) materials are the most promising candidates for nanoscale spintronics, which can fulfill the demand of independent control of charge and spin.[6–8] The Mermin–Wagner theorem shows that no 2D long-range isotropic ferromagnetism would exist with continuous spin symmetries at finite temperatures.[9] The discoveries of 2D long-range ferromagnetic (FM) order with thickness down to the atomic limit in van der Waals (vdWs) crystals CrI_3 and $Cr_2Ge_2Te_6$ have completely disrupted the Mermin–Wagner theory and opened new platforms for studying nanoscale spintronic devices.[10,11] Since then, more 2D FMS materials have been observed experimentally and predicted theoretically.[6–8,12–27] Further analysis shows that magnetic anisotropy (MA) is the prerequisite and foundation to verify whether a 2D material exhibits a magnetically ordered phase above zero temperature,[28–30] and the 2D FM order can be stabilized by the magnon excitation gap caused by uniaxial magnetic anisotropy.[31–33] MA, which can be scaled by the magnetic anisotropy energy (MAE), is mainly determined by two factors; one is the magnetocrystalline anisotropy resulting from the spin–orbit coupling interaction (SOC-MAE) and the other is the shape anisotropy caused by the dipole–dipole interaction (shape-MAE).[34] Compared with the SOC-MAE, the shape-MAE is often relatively weak and of less concern. But for a 2D system with a weak SOC-MAE, the shape-MAE may have an important contribution. The larger the total MAE (sum of SOC-MAE and shape-MAE), the stronger the resistance of magnetic ordering against thermal fluctuations, which can improve the stability of magnetic states.[35] However, a detailed microscopic analysis of total MAE received little attention previously.

Recently, a promising 2D van der Waals semiconducting magnet, CrSBr, is of great interest owing to its exotic properties.[12,25,36–50] Bulk CrSBr is a layered A-type antiferromagnetic semiconductor with the Néel temperature $T_N \approx 140$ K, and it exhibits triaxial magnetic anisotropy (intermediate magnetization *x* axis, easy magnetization *y* axis, and hard magnetization *z* axis) with a band gap of about 1.5 eV.[25,44,49]

Joint Center for Theoretical Physics, School of Physics and Electronics, Henan University, Kaifeng 475004, People's Republic of China.
E-mail: gbzhang@vip.henu.edu.cn, 20130016@vip.henu.edu.cn, cliu@vip.henu.edu.cn

† Electronic supplementary information (ESI) available. See DOI: https://doi.org/10.1039/d3nr02518g

More importantly, CrSBr exhibits air stability and gate-tunable conductivity, which reinforces its potential application as a spintronic device.[50] In 2018, we predicted the possibility of a CrSBr monolayer stripping from its bulk, and it is a high-temperature ferromagnetic semiconductor with a T_C of 160 K.[12] Then, the T_C of the CrSBr monolayer was also predicted to be 290 K using the Ising model[51] and 124 K using the anisotropic Heisenberg model.[16] Yang *et al.* calculated the T_C of the CrSBr monolayer to be 175 K.[36] Very recently, CrSBr monolayers have been experimentally confirmed using the second harmonic generation technique, and the measured T_C is about 146 K.[25] Besides, considering the small value of MAE (below meV) and the outstanding deformation capacity of 2D materials, it is easily affected by external strains. Strain engineering has also been proved to be a powerful tool to tune the properties of 2D materials, which has been able to induce switching between indirect and direct band-gap semiconductors[52,53] and between antiferromagnetic (AFM) and FM states,[54–56] induce phase transition,[57–59] *etc*. Therefore, the effect of strain on MA is also necessary to be explored because of the importance of magnetic anisotropy in the context of 2D magnetism.

Motivated by these burgeoning developments, we focus on the recently observed 2D air-stable FMS CrSBr monolayer.[25,43] First, using the first-principles calculations, the triaxial magnetic MA of bulk CrSBr, which was confirmed experimentally, was well reproduced.[36,45,49] Interestingly, the CrSBr monolayer also exhibits triaxial MA, which originates from the coexistence of spin–orbit coupling and dipole–dipole interactions. The contribution of the dipole–dipole interaction to MA is much more important than that of the spin–orbit coupling interaction. Under strains, the intermediate magnetization, easy magnetization, and hard magnetization axes can be converted to each other, providing an ideal candidate material for triaxial magnetic switching. Besides, by using the four ordered spin state method, the value of T_C measured using the experiment was well reproduced and can be further increased by applying strains. Our findings not only provide a detailed understanding of 2D magnetism in the CrSBr monolayer, but also explore an effective strategy to control the MA and enhance the T_C.

Method

Spin-polarized calculations are adopted within the framework of the density functional theory, especially implemented in the Vienna *ab initio* simulation package (VASP).[60] The projector augmented wave (PAW) pseudopotential method with an energy cutoff of 500 eV is used to describe the interaction between electrons and atomic nuclei.[61] The electronic exchange correlation function is expressed by the Perdew–Burke–Ernzerhof (PBE) functional under the generalized gradient approximation (GGA).[62] The convergence criterion is 10^{-6} eV for total energies and 0.01 eV Å^{-1} for force. A vacuum layer of about 25 Å is added to prevent the interaction between layers.[63] The PBE + U approach was used to describe the strong correlation effect for the 3d orbital of the Cr atom, in which the values of U and J are 4.03 eV and 0.96 eV, respectively.[47]

Total MAE is the sum of SOC-MAE and shape-MAE. The calculation of SOC-MAE is based on the second-order perturbation theory, and the Hamiltonian containing spin–orbit coupling interaction (SOC) can be written as:

$$H^{\mathrm{SOC}} = \lambda^2 \left(\sum_{m \neq n} \frac{\left| \langle \uparrow, n | \hat{\boldsymbol{S}} \cdot \hat{\boldsymbol{L}} | \uparrow, m \rangle \right|^2}{E_n^{(0)} - E_m^{(0)}} \right) + \sum_{m \neq n} \frac{\left| \langle \uparrow, n | \hat{\boldsymbol{S}} \cdot \hat{\boldsymbol{L}} | \downarrow, m \rangle \right|^2}{E_n^{(0)} - E_m^{(0)}} + \sum_{m \neq n} \frac{\left| \langle \downarrow, n | \hat{\boldsymbol{S}} \cdot \hat{\boldsymbol{L}} | \uparrow, m \rangle \right|^2}{E_n^{(0)} - E_m^{(0)}} + \sum_{m \neq n} \frac{\left| \langle \downarrow, n | \hat{\boldsymbol{S}} \cdot \hat{\boldsymbol{L}} | \downarrow, m \rangle \right|^2}{E_n^{(0)} - E_m^{(0)}}$$

where λ is the SOC constant, $|\uparrow\rangle$ and $|\downarrow\rangle$ denote the spin-up and spin-down states, respectively, $|n\rangle$ and $|m\rangle$ represent the eigenstates of the Hamiltonian operator respectively, $E_n^{(0)}$ and $E_m^{(0)}$ correspond to the eigenvalues of the eigenstates respectively, and $\hat{\boldsymbol{S}}$ and $\hat{\boldsymbol{L}}$ correspond to the spin momentum operator and orbital angular momentum operator, respectively. All the derivations are provided in the ESI.† The shape-MAE is caused by the dipole–dipole interaction and is expressed as:

$$E^{\mathrm{dip-dip}} = \frac{1}{2} \frac{\mu_0}{4\pi} \sum_{q \neq q'}^{N} \frac{1}{{r_{qq'}}^3} \left[M_q M_{q'} - \frac{3}{{r_{qq'}}^2} (M_q \cdot r_{qq'})(M_{q'} \cdot r_{qq'}) \right]$$

where μ_0 is the permeability of vacuum, q is the atomic coordinate of the Cr atom, r is the distance between two magnetic atoms, and M represents the magnetic moment. According to the formula, shape-MAE is only related to the position and magnetic moment of magnetic atoms.

Results and discussion

The optimized lattice constants of the CrSBr monolayer are a = 3.59 Å and b = 4.82 Å, which are in good agreement with previous studies.[12,25] The FM and four AFM states are considered for the CrSBr monolayer (Fig. S1†), and the results show that the FM state is the ground state, which is consistent with the experimental result.[25] Magnetism mainly stems from the Cr atoms with a magnetic moment of $3\mu_B$ while the S/Br atoms hold a small opposite magnetic moment, which was shown in the spin density distribution (Fig. 1b).

Analysis of the band structure shows that the CrSBr monolayer is a ferromagnetic semiconductor with an indirect bandgap of about 1.35 eV (Fig. 2a), which is in good agreement with the optical band gap measured in the experiment (1.25 ± 0.07 eV).[25] Detailed analysis of the atomic-resolved band structure illustrates that the conduction band around the Fermi level is dominated by orbitals of Cr atoms, whereas the valence band is dominated by hybridized orbitals of Br and S atoms, which agree with the results of the density of states (DOS) as shown in Fig. S2.† Analysis of the orbital-resolved DOS shows that the conduction band minima and valence band maxima are mainly occupied by the $d_{x^2-y^2}$ orbits of the Cr atom and p_y orbits of S and Br, respectively.

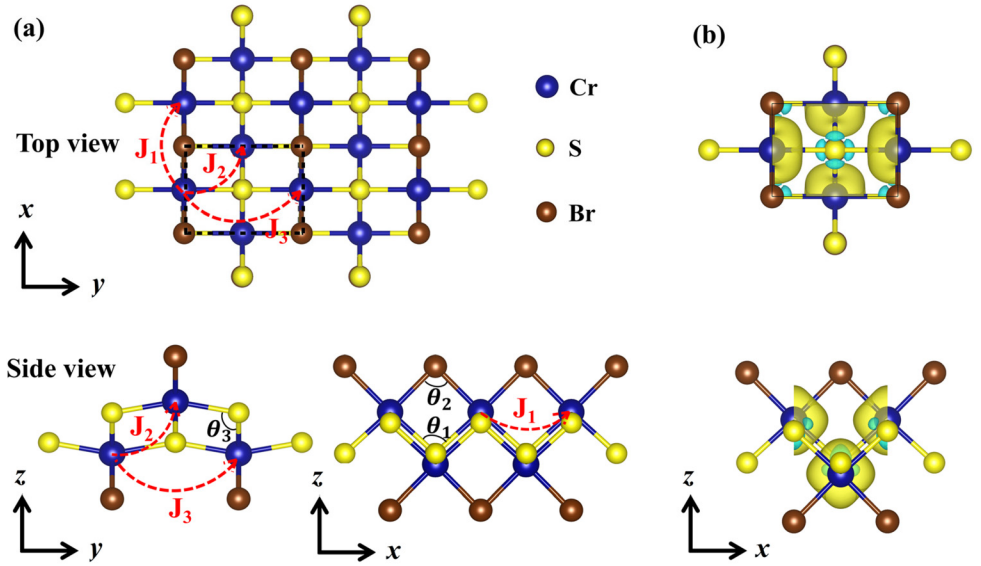

Fig. 1 (a) The top view and side view of the CrSBr monolayer. (b) Spin density of the CrSBr monolayer.

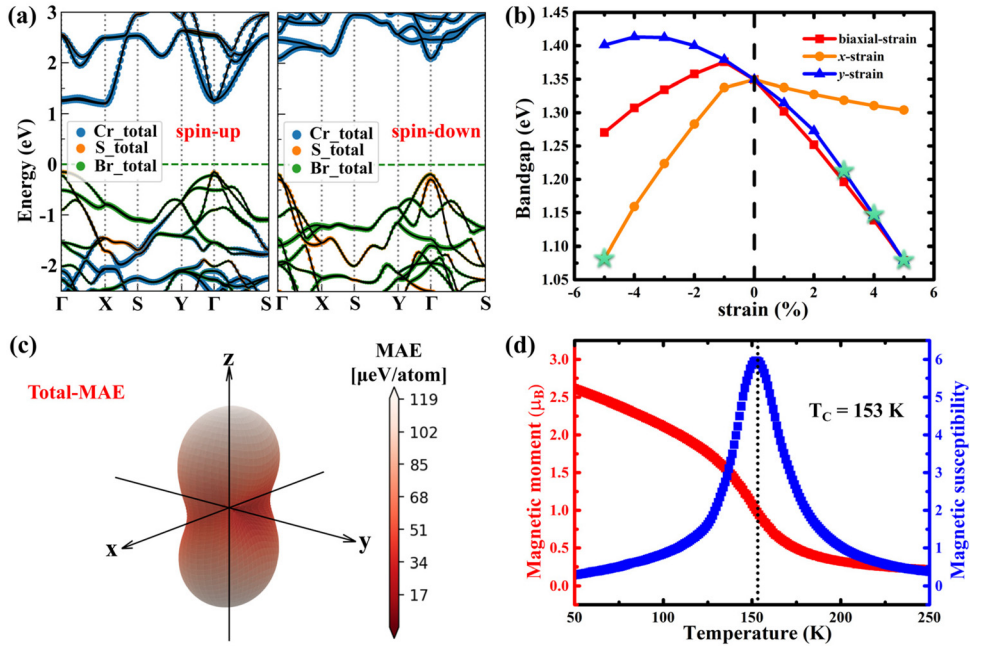

Fig. 2 (a) The band structure of the CrSBr monolayer. (b) The band gaps of the CrSBr monolayer under biaxial and uniaxial strains (−5%–5%). The star represents a direct bandgap. (c) Angular dependence of the total-MAE of the CrSBr monolayer with the direction of magnetization lying on the whole space. (d) The magnetic moment and magnetic susceptibility as functions of temperature for the CrSBr monolayer.

Fig. S3† shows that the CrSBr monolayer remains in ferromagnetic order under compression and tension strains (from −5% to 5%) and the strain has little effect on the lattice structures and magnetic moment. By applying external strain along different directions, the band-gap of the CrSBr monolayer can be flexibly adjusted from about 1 eV to 1.4 eV (Fig. 2b). Interestingly, an increase in strain along the x and y directions is accompanied by a shift from an indirect to a direct band gap (Fig. 2b). The detailed band structure of the CrSBr monolayer under different strains is shown in Fig. S4–S6.† The reason may be that the applied strain causes a splitting of the band along the X–Γ direction and changes the position of the conduction band bottom from the X to the Γ point.

The magnetocrystalline anisotropy energy (SOC-MAE) of CrSBr bulk was first calculated using the second-order perturbation theory in three directions (the [100], [010], and [001]

Table 1 The SOC-MAE, shape-MAE, and total-MAE (μeV/Cr) of the CrSBr bulk and monolayer along the [100], [010], and [001] directions, respectively, which is referenced to the energy of the [010] direction

		$E_{[100]}$	$E_{[010]}$	$E_{[001]}$	Energy order of magnetic axes
Bulk	SOC-MAE	8	−32	0	$y < z < x$
	Shape-MAE	−59	−40	0	$x < y < z$
	Total-MAE	−51	−72	0	$y < x < z$
					$y < x < z$ (exp.[49,64])
Monolayer	SOC-MAE	24	−55	0	$y < z < x$
	Shape-MAE	−75	−64	0	$x < y < z$
	Total-MAE	−51	−119	0	$y < x < z$

directions) as shown in Table 1. Obviously, the energy of the y axis (the [010] direction) is lower than that of the z axis (the [001] direction), and the x axis (the [100] direction) has the highest energy (the energy order is $y < z < x$). This is not consistent with the results of the experiment ($y < x < z$), which shows that bulk CrSBr exhibits the easy y axis, intermediate x axis, and hard z axis.[38,40,49,64] Although the calculated easy magnetic axis is the same as the experimental result (the [010] direction), the measured triaxial MAE by experiment is not well reproduced. Compared to the weak SOC-MAE, shape anisotropy induced by the magnetic dipole–dipole interaction may have an important contribution (shape-MAE).[65] The in-plane shape-MAE was also calculated (Table 1), in which r_{max} = 3000 Å was used to ensure the numerical reliability. Interestingly, after considering the magnetic dipole–dipole interaction, the total-MAE (sum of SOC-MAE and shape-MAE) shows that y, x, and z are indeed the easy, the intermediate, and the hard axis, respectively, reflecting its triaxial anisotropy. These results not only well reproduce the experimental triaxial MAE of bulk, but also demonstrate the important role of the magnetic dipole–dipole interaction (shape-MAE) in this material.

The SOC-MAE and shape-MAE of the CrSBr monolayer were also calculated (Table 1), and the results show that this monolayer also possesses triaxial magnetic anisotropy. Moreover, the value of shape-MAE is larger than that of SOC-MAE. The presence of triaxial magnetic anisotropy in the CrSBr monolayer is different from the present in-plane and out-of-plane magnets,[7,66] reinforcing the interest in the CrSBr monolayer as a potential host for exotic magnetic states. In order to show more clearly this novel property, the angular dependences of SOC-MAE, shape-MAE, and total-MAE along the three planes (the xz plane, yz plane, and xy plane) and the whole space are presented in Fig. S7† and Fig. 2c. Clearly, the MAE strongly depends on the direction of magnetization in the whole space, which confirms again the strong magnetic anisotropy in this monolayer.

Fig. 3 shows the variation of SOC-MAE, shape-MAE, and total-MAE of the CrSBr monolayer under biaxial and uniaxial strains. The trend of energy change in Fig. 3a is almost the

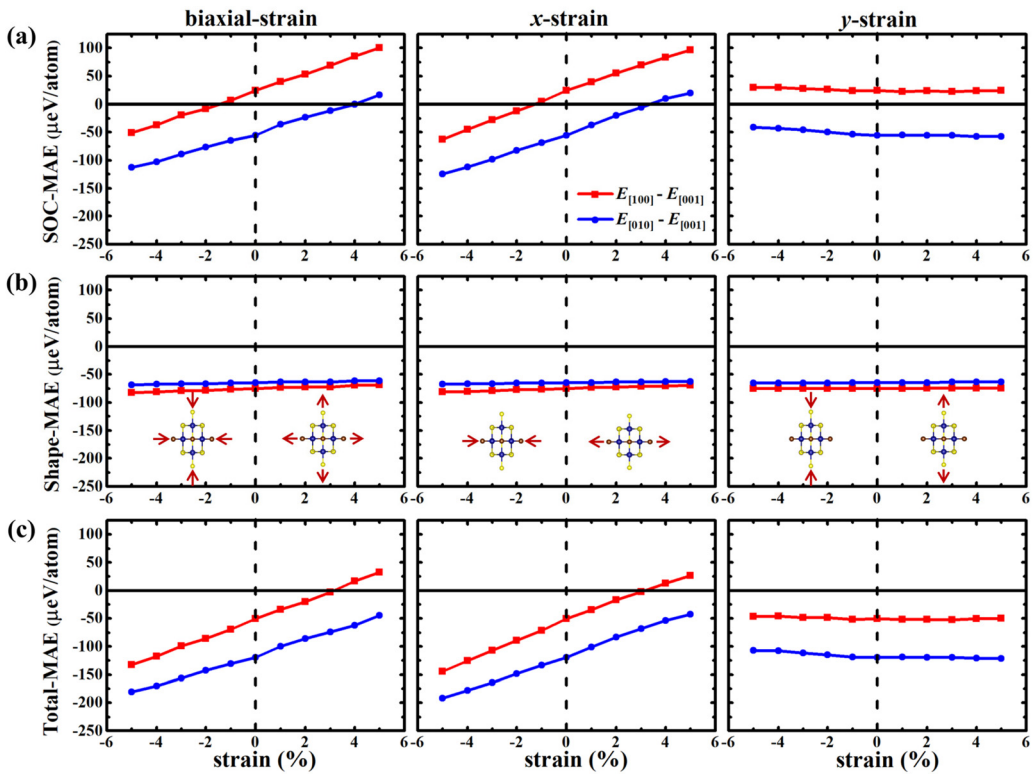

Fig. 3 Variation of the SOC-MAE (a), shape-MAE (b), and total-MAE (c) of the CrSBr monolayer under biaxial and uniaxial strains (−5%–5%). The energy is the reference along the [001] direction.

same under the biaxial strains and uniaxial strains along the *x* direction, while the relative energy is almost constant under strains along the *y* direction, suggesting the SOC-MAE is sensitive to the strains along the *x* direction. Fig. 3b shows that the effect of strains on the values of shape-MAE is negligible because of the small changes in the crystal structure and magnetic moment under different strains. Under different strains, Fig. 3c shows the variation of total MAE. Clearly, the variation trend of total-MAE in Fig. 3a and c is consistent, suggesting that the change in the total-MAE is mainly caused by the spin–orbit coupling under different strains, especially the uniaxial strain along the *x* direction. The corresponding SOC-MAE and total-MAEs through the whole space under different uniaxial strains are plotted in Fig. 4 and Fig. S8, S9.† These figures further confirm that the CrSBr monolayer has strong triaxial magnetic anisotropy and the MAE is most sensitive to uniaxial strain along the *x* direction.

To further elucidate the origin of the strain effect on the SOC-MAE, we first determine separate contributions of the Cr, S and Br atoms to SOC-MAE (Fig. S10†). The results show that the SOC-MAE is mainly contributed by the Cr_d orbitals and Br_p orbitals, which are the most sensitive to external strain. Taking a biaxial tensile strain of 5% as an example, Fig. S10a† shows that the contribution of Cr_d orbitals to the MAE between the [100] and [001] direction is much more than that of the other orbitals. Fig. S10b† shows that the MAE between the directions [010] and [100] is mainly contributed by the Cr_d orbitals and Br_p orbitals. The values of SOC-MAE, of each d orbital of Cr_d orbitals (including d_{xy}, d_{yz}, d_{z^2}, d_{xz}, and $d_{x^2-y^2}$) and the individual p orbitals of Br_p (including p_y, p_z, and p_x) were also calculated. Fig. 5 and S11–S15† represent the amount of energy change in the [100], [010] and [001] directions for individual Cr_d and Br_p orbitals under biaxial, *x*-directional uniaxial and *y*-directional uniaxial strains,

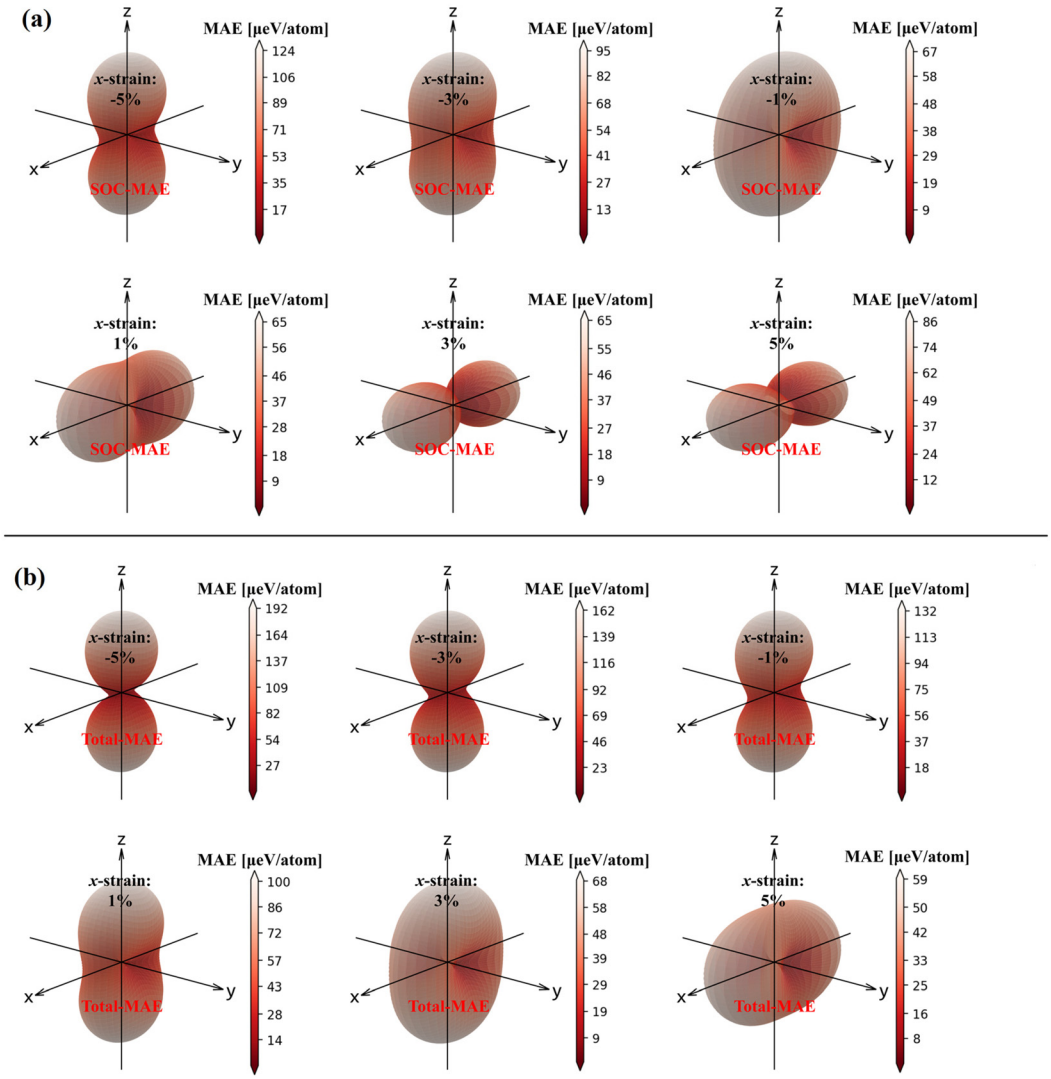

Fig. 4 The variation of SOC-MAE (a) and total-MAE (b) for the CrSBr monolayer in the whole space under uniaxial *x* strain (−5%–5%).

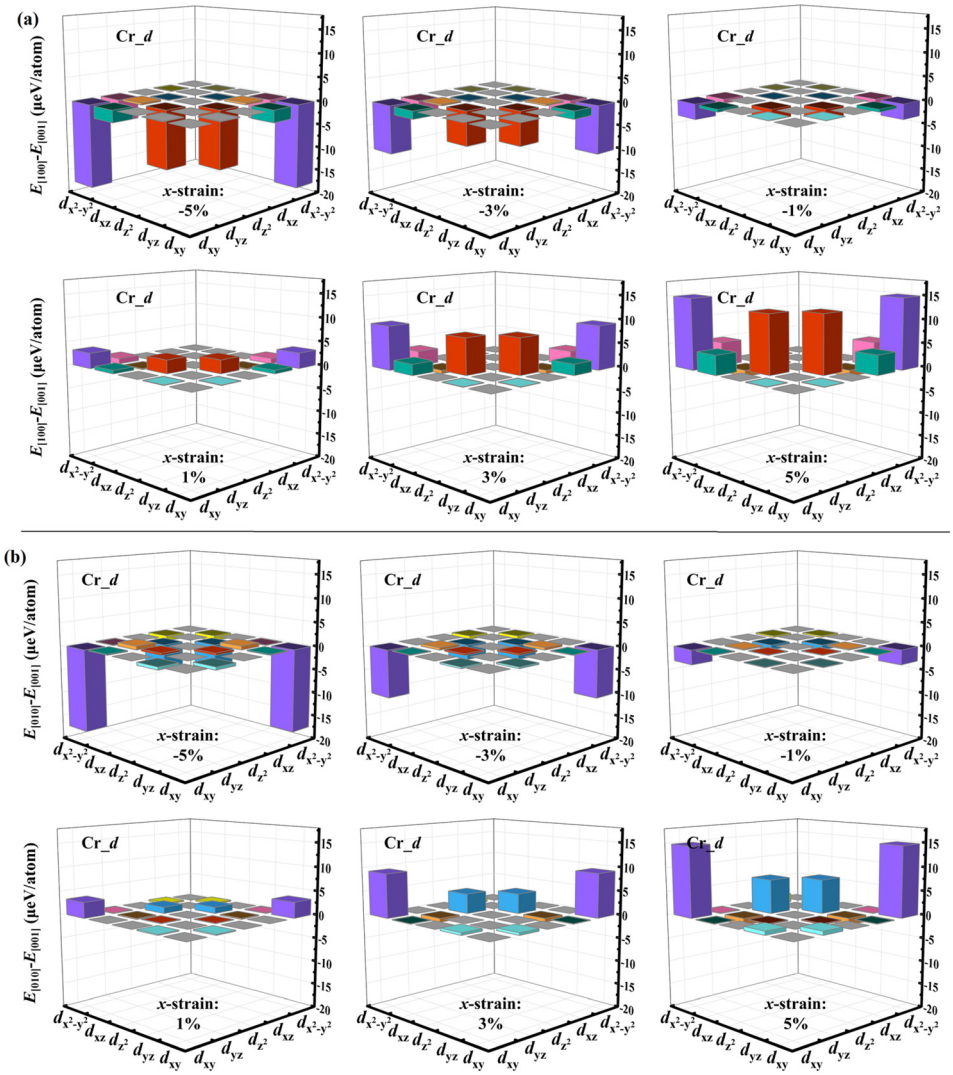

Fig. 5 The contribution to MAE from the SOC interaction between different d orbital channels for Cr atoms under different uniaxial *x* strains along the [100] (a) and the [010] (b) directions. The energy is the reference along the [001] direction.

respectively. These figures reveal that the coupling between Cr_$d_{x^2-y^2}$ and Cr_d_{xy} orbitals and that between Cr_d_{z^2} and Cr_d_{yz} orbitals are more sensitive to biaxial strain and uniaxial in the *x*-direction. According to the formula and Tables S3 and S4 given in the ESI,† the Cr_$d_{x^2-y^2}$ and Cr_d_{xy} coupling through $\hat{l}_x$ and $\hat{l}_y$ in the same spin state and that in different spin states are both equal to 0, while the coupling of these two orbits *via* $\hat{l}_z$ in the same spin state is not 0, which indicates that the coupling between Cr_$d_{x^2-y^2}$ and Cr_d_{xy} will provide a higher spin orbit coupling energy in the *z* direction. Similarly, the coupling between Cr_d_{z^2} and Cr_d_{yz} orbitals gain a nonzero value only *via* $\hat{l}_x$ for different spin states, suggesting that the coupling of Cr_d_{z^2} and Cr_d_{yz} orbitals will provide a low spin orbit coupling energy in the *y* and *z* directions. The coupling of other orbits can also be derived in the same way according to Tables S3 and S4.† Taking the example of *x* direction tensile strain, the enhancement of tensile strain weakens the coupling strength of Cr_$d_{x^2-y^2}$ and Cr_d_{xy} *via* $\hat{l}_z$ in the same spin state, while at the same time, Cr_d_{z^2} and Cr_d_{yz} orbitals in the same spin state *via* $\hat{l}_x$ coupling in different spin states and Cr_d_{z^2} and Cr_d_{xz} orbitals *via* $\hat{l}_y$ in different states are both enhanced, eventually resulting in the lowest energy in the *z* direction. In addition, the SOC-MAE of individual p-orbitals of the Br atom is less sensitive to strain than that of the individual Cr_d orbitals and the energy change is within 5 μeV. The angular momentum coupling through the individual p-orbitals can also be obtained according to the formula and Table S3 in the ESI.† We also take the example of *x*-direction tensile strain. The strengthening of the tensile strain is accompanied by a weakening of the $\hat{l}_z$ coupling between Br_p_x and Br_p_y in the same spin state, a weakening of the $\hat{l}_x$ coupling between Br_p_y and Br_p_z in the same spin state, and a strengthening of the $\hat{l}_y$ coupling between Br_p_x and Br_p_z in the same spin state.

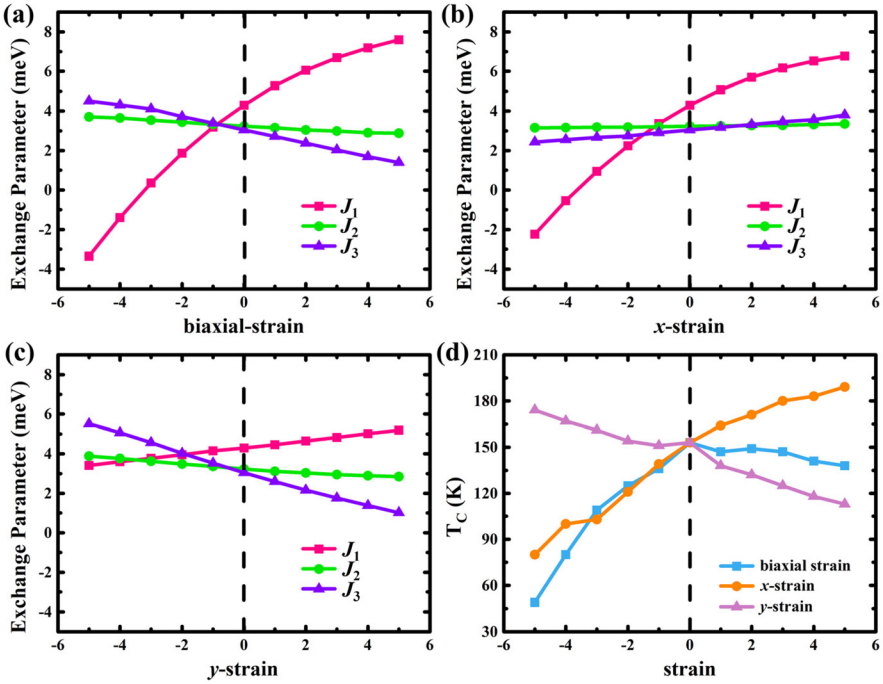

Fig. 6 Variation of exchange parameters with biaxial strain (a), uniaxial strain in the *x*-direction (b), and uniaxial in the *y*-direction (c), respectively. (d) The changes of T_C at different strains.

Because of the importance of T_C for the application of 2D magnets, we estimated the T_C of the CrSBr monolayer using Monte Carlo simulations based on the Heisenberg model, and the Hamiltonian can be written as

$$H = -\frac{1}{2}\sum_{k=1,2,3} J_k \sum_{i,j} \boldsymbol{S}_i \boldsymbol{S}_j + A\sum_i (S_i^z)^2$$

where J_k (k = 1, 2, 3) represents the magnetic exchange parameters of the nearest neighbor, the second-neighbor, and the third-neighbor between pairs of spins, respectively (Fig. 1). $\boldsymbol{S}_i$ or $_j$ stands for the spin vector, and S_i^z is the spin component along the *z*-axis. A represents the anisotropy parameter. By using four ordered spin states, J_k was calculated on the basis of density-functional calculations.[67] The values of J_1, J_2 and J_3 for the CrSBr monolayer are 4.29, 3.23 and 3.04 meV respectively. The result shows that the T_C of the CrSBr monolayer is about 153 K (Fig. 2d), which is in excellent agreement with the experimental result (146 K).[25] The T_C is higher than that of other successfully prepared 2D ferromagnetic semiconductors, such as CrX_3 (X = Cl, Br, I) monolayers (27 K, 40 K, and 45 K)[7] and $Cr_2Ge_2Te_6$ bilayers (28 K).[11] The strain-dependent evolution of magnetic exchange parameters (J_1, J_2, and J_3) was also investigated and is shown in Fig. 6a–c. Due to the asymmetric structure of the CrSBr monolayer, J_1, J_2, and J_3 exhibit independent evolution depending on the crystallographic direction of the applied strain. The results show that J_2 and J_3 have a roughly similar trend in the whole strain while J_1 was strongly influenced by the uniaxial stain in the *x*-direction. Moreover, the strain enables the adjustment of T_C in the range of 49 to 189 K (Fig. 6d), and the calculated magnetic moment and susceptibility as functions of temperature for the CrSBr monolayer under biaxial and uniaxial strains are also illustrated in Fig. S16S18.†

Summary

In summary, we have investigated the origin of triaxial anisotropic magnetic properties of the air-stable 2D magnetic semiconductor CrSBr using first-principles calculations. The CrSBr monolayer exhibits triaxial anisotropy, which originates from the coexistence of the magnetic dipole–dipole interaction (shape anisotropy) and the spin–orbit coupling interaction (magnetocrystalline anisotropy), and we also unveil that the magnetic shape anisotropy, which has been neglected in most previous works, is of importance for works of weak magnetocrystalline anisotropy. Interestingly, the energy order of the three magnetic axes of the CrSBr monolayer can be tuned by applying strains, in which the SOC-MAE is more sensitive to strains than shape-MAE. Further analysis shows that the enhancement of biaxial and uniaxial *x*-direction tensile strain weakens the coupling strength of Cr_$d_{x^2-y^2}$ and Cr_d_{xy} *via* $\hat{l}_z$ in the same spin state while enhancing the coupling strength of Cr_d_{z^2} and Cr_d_{yz} *via* $\hat{l}_x$ in different spin states and Cr_d_{z^2} and Cr_d_{xz} *via* $\hat{l}_y$ in different spin states, eventually achieving triaxial switching in the process. Besides, the strains also can flexibly adjust the band gap and even change the original indirect band gap to a direct band gap. By using the four ordered spin states, the observed T_C (146 K) of the CrSBr monolayer is well

reproduced based on Monte Carlo simulations (152 K) and the T_C can be increased to 189 K under uniaxial strain in the x direction. Our work gives insights into understanding the MAE of 2D ferromagnetism and paves the way for strain control of switchable magnetic anisotropy and Curie temperature for exploring new spintronic applications.

Author contributions

B. Wang: formal analysis, writing – original draft, and funding acquisition; Y. Wu: formal analysis, writing – original draft, and data curation; Y. Bai: supervision and writing – original draft; P. Shi: data curation; G. Zhang: visualization, methodology and funding acquisition; Y. Zhang: writing – review & editing and funding acquisition, C. Liu: writing – review & editing and project administration. All authors checked the manuscript.

Conflicts of interest

There are no conflicts to declare.

Acknowledgements

This work was financially supported by the National Natural Science Foundation of China (no. 12047517, 12104130, and 11904079), the China Postdoctoral Science Foundation (no. 2020M682274 and 2020TQ0089), the Postgraduate Education Reform and Quality Improvement Project of Henan Province (grant no. YJS2023ZX19), the Scientific Research Key Project Fund of Henan Provincial Education Department (no. 23B140005), and the Innovative Experimental Training Program for College Students of Henan University (no. 20231011011).

References

1 Y. Liu, C. Zeng, J. Zhong, J. Ding, Z. M. Wang and Z. Liu, *Nano-Micro Lett.*, 2020, **12**, 1–26.
2 Y. Tu, Q. Liu, L. Hou, P. Shi, C. Jia, J. Su, J. Zhang, X. Zhang and B. Wang, *Front. Phys.*, 2022, **10**, 1078202.
3 Y. P. Feng, L. Shen, M. Yang, A. Wang, M. Zeng, Q. Wu, S. Chintalapati and C.-R. Chang, *Wiley Interdiscip. Rev.: Comput. Mol. Sci.*, 2017, **7**, e1313.
4 X. Li and J. Yang, *Natl. Sci. Rev.*, 2016, **3**, 365–381.
5 S. Xing, J. Zhou, X. Zhang, S. Elliott and Z. Sun, *Prog. Mater. Sci.*, 2022, 101036.
6 X. Li and J. Yang, *J. Am. Chem. Soc.*, 2019, **141**, 109–112.
7 B. Wang, X. Zhang, Y. Zhang, S. Yuan, Y. Guo, S. Dong and J. Wang, *Mater. Horiz.*, 2020, **7**, 1623–1630.
8 C. Huang, J. Feng, F. Wu, D. Ahmed, B. Huang, H. Xiang, K. Deng and E. Kan, *J. Am. Chem. Soc.*, 2018, **140**, 11519–11525.
9 N. D. Mermin and H. Wagner, *Phys. Rev. Lett.*, 1966, **17**, 1133–1136.
10 B. Huang, G. Clark, E. Navarro-Moratalla, D. R. Klein, R. Cheng, K. L. Seyler, D. Zhong, E. Schmidgall, M. A. McGuire, D. H. Cobden, W. Yao, D. Xiao, P. Jarillo-Herrero and X. Xu, *Nature*, 2017, **546**, 270–273.
11 C. Gong, L. Li, Z. Li, H. Ji, A. Stern, Y. Xia, T. Cao, W. Bao, C. Wang, Y. Wang, Z. Q. Qiu, R. J. Cava, S. G. Louie, J. Xia and X. Zhang, *Nature*, 2017, **546**, 265–269.
12 Y. Guo, Y. Zhang, S. Yuan, B. Wang and J. Wang, *Nanoscale*, 2018, **10**, 18036–18042.
13 V. V. Kulish and W. Huang, *J. Mater. Chem. C*, 2017, **5**, 8734–8741.
14 X. Cai, T. Song, N. P. Wilson, G. Clark, M. He, X. Zhang, T. Taniguchi, K. Watanabe, W. Yao, D. Xiao, M. A. McGuire, D. H. Cobden and X. Xu, *Nano Lett.*, 2019, **19**, 3993–3998.
15 H. H. Kim, B. Yang, S. Li, S. Jiang, C. Jin, Z. Tao, G. Nichols, F. Sfigakis, S. Zhong and C. Li, *Proc. Natl. Acad. Sci. U. S. A.*, 2019, **116**, 11131–11136.
16 C. Wang, X. Zhou, L. Zhou, N.-H. Tong, Z.-Y. Lu and W. Ji, *Sci. Bull.*, 2019, **64**, 293–300.
17 K. Sheng, Q. Chen, H.-K. Yuan and Z.-Y. Wang, *Phys. Rev. B*, 2022, **105**, 075304.
18 Y. Wu, W. Sun, S. Liu, B. Wang, C. Liu, H. Yin and Z. Cheng, *Nanoscale*, 2021, **13**, 16564–16570.
19 W. Liu, J. Tong, L. Deng, B. Yang, G. Xie, G. Qin, F. Tian and X. Zhang, *Mater. Today Phys.*, 2021, **21**, 100514.
20 J.-Y. You, Z. Zhang, X.-J. Dong, B. Gu and G. Su, *Phys. Rev. Res.*, 2020, **2**, 013002.
21 Y. Ren, Q. Li, W. Wan, Y. Liu and Y. Ge, *Phys. Rev. B*, 2020, **101**, 134421.
22 Z. S. Zhang, J. Jiang, C. Rasmita, A. Gao, W. Yu and T. Yu, *Nano Lett.*, 2019, **19**, 3138–3142.
23 S. Lu, Q. Zhou, Y. Guo and J. Wang, *Chem*, 2022, **8**, 769–783.
24 H. H. Kim, B. Yang, S. Li, S. Jiang, C. Jin, Z. Tao, G. Nichols, F. Sfigakis, S. Zhong, C. Li, S. Tian, D. G. Cory, G. X. Miao, J. Shan, K. F. Mak, H. Lei, K. Sun, L. Zhao and A. W. Tsen, *Proc. Natl. Acad. Sci. U. S. A.*, 2019, **116**, 11131–11136.
25 K. Lee, A. H. Dismukes, E. J. Telford, R. A. Wiscons, J. Wang, X. Xu, C. Nuckolls, C. R. Dean, X. Roy and X. Zhu, *Nano Lett.*, 2021, **21**, 3511–3517.
26 H. Y. Lv, W. J. Lu, X. Luo, X. B. Zhu and Y. P. Sun, *Phys. Rev. B*, 2019, **99**, 134416.
27 J. Y. Chen, X. X. Li, W. Z. Zhou, J. L. Yang, F. P. Ouyang and X. Xiong, *Adv. Electron. Mater.*, 2020, **6**, 1900490.
28 C. Xu, J. Feng, H. Xiang and L. Bellaiche, *npj Comput. Mater.*, 2018, **4**, 1–6.
29 Y. Yue, *J. Supercond. Novel Magn.*, 2016, **30**, 1201–1206.
30 S. D. Guo, Y. L. Tao, K. Cheng, B. Wang and Y. S. Ang, *J. Phys.: Condens. Matter*, 2022, **34**, 505802.
31 G. Zhang, F. Guo, H. Wu, X. Wen, L. Yang, W. Jin, W. Zhang and H. Chang, *Nat. Commun.*, 2022, **13**, 5067.
32 Y. Bai, R. Shi, Y. Wu, B. Wang and X. Zhang, *J. Phys.: Condens. Matter*, 2022, **34**, 384001.

33 C. Gong and X. Zhang, *Science*, 2019, **363**, eaav4450.
34 J. Su, Y. Bai, P. Shi, Y. Tu and B. Wang, *Results Phys.*, 2023, **51**, 106635.
35 B. Xu, S. Li, K. Jiang, J. Yin, Z. Liu, Y. Cheng and W. Zhong, *Appl. Phys. Lett.*, 2020, **116**, 052403.
36 K. Yang, G. Wang, L. Liu, D. Lu and H. Wu, *Phys. Rev. B*, 2021, **104**, 144416.
37 Y. J. Bae, J. Wang, A. Scheie, J. Xu, D. G. Chica, G. M. Diederich, J. Cenker, M. E. Ziebel, Y. Bai, H. Ren, C. R. Dean, M. Delor, X. Xu, X. Roy, A. D. Kent and X. Zhu, *Nature*, 2022, **609**, 282–286.
38 C. Boix-Constant, S. Manas-Valero, A. M. Ruiz, A. Rybakov, K. A. Konieczny, S. Pillet, J. J. Baldovi and E. Coronado, *Adv. Mater.*, 2022, **34**, 2204940.
39 J. Cenker, S. Sivakumar, K. Xie, A. Miller, P. Thijssen, Z. Liu, A. Dismukes, J. Fonseca, E. Anderson, X. Zhu, X. Roy, D. Xiao, J. H. Chu, T. Cao and X. Xu, *Nat. Nanotechnol.*, 2022, **17**, 256–261.
40 T. M. J. Cham, S. Karimeddiny, A. H. Dismukes, X. Roy, D. C. Ralph and Y. K. Luo, *Nano Lett.*, 2022, **22**, 6716–6723.
41 D. L. Esteras, A. Rybakov, A. M. Ruiz and J. J. Baldoví, *Nano Lett.*, 2022, **22**, 8771–8778.
42 J. Klein, T. Pham, J. D. Thomsen, J. B. Curtis, T. Denneulin, M. Lorke, M. Florian, A. Steinhoff, R. A. Wiscons, J. Luxa, Z. Sofer, F. Jahnke, P. Narang and F. M. Ross, *Nat. Commun.*, 2022, **13**, 5420.
43 W. Liu, X. Guo, J. Schwartz, H. Xie, N. U. Dhale, S. H. Sung, A. L. N. Kondusamy, X. Wang, H. Zhao, D. Berman, R. Hovden, L. Zhao and B. Lv, *ACS Nano*, 2022, **16**, 15917–15926.
44 S. A. Lopez-Paz, Z. Guguchia, V. Y. Pomjakushin, C. Witteveen, A. Cervellino, H. Luetkens, N. Casati, A. F. Morpurgo and F. O. von Rohr, *Nat. Commun.*, 2022, **13**, 4745.
45 D. J. Rizzo, A. S. McLeod, C. Carnahan, E. J. Telford, A. H. Dismukes, R. A. Wiscons, Y. Dong, C. Nuckolls, C. R. Dean and A. N. Pasupathy, *Adv. Mater.*, 2022, **34**, 2201000.
46 A. Scheie, M. Ziebel, D. G. Chica, Y. J. Bae, X. Wang, A. I. Kolesnikov, X. Zhu and X. Roy, *Adv. Sci.*, 2022, **9**, e2202467.
47 X. Yang, P. Yang, X. Zhou, W. Feng and Y. Yao, *Phys. Rev. B*, 2022, **106**, 054408.
48 C. Ye, C. Wang, Q. Wu, S. Liu, J. Zhou, G. Wang, A. Soll, Z. Sofer, M. Yue, X. Liu, M. Tian, Q. Xiong, W. Ji and X. R. Wang, *ACS Nano*, 2022, **16**, 11876–11883.
49 E. J. Telford, A. H. Dismukes, K. Lee, M. Cheng, A. Wieteska, A. K. Bartholomew, Y. S. Chen, X. Xu, A. N. Pasupathy and X. Zhu, *Adv. Mater.*, 2020, **32**, 2003240.
50 S. A. López-Paz and F. O. von Rohr, *Chimia*, 2022, **76**, 628.
51 Z. Jiang, P. Wang, J. Xing, X. Jiang and J. Zhao, *ACS Appl. Mater. Interfaces*, 2018, **10**, 39032–39039.
52 S. Zhang, Z. Yan, Y. Li, Z. Chen and H. Zeng, *Angew Chem., Int. Ed.*, 2015, **54**, 3112–3115.
53 J. Hu, P. Wang, J. Zhao and R. Wu, *Adv. Phys.: X*, 2018, **3**, 1432415.
54 S. Li, Z. Ao, J. Zhu, J. Ren, J. Yi, G. Wang and W. Liu, *J. Phys. Chem. Lett.*, 2017, **8**, 1484–1488.
55 Y. Wang, S. S. Wang, Y. Lu, J. Jiang and S. A. Yang, *Nano Lett.*, 2016, **16**, 4576–4582.
56 C. Liu, B. Fu, H. Yin, G. Zhang and C. Dong, *Appl. Phys. Lett.*, 2020, **117**, 103101.
57 P. Liu, S. Liu, M. Jia, H. Yin, G. Zhang, F. Ren, B. Wang and C. Liu, *Appl. Phys. Lett.*, 2022, **121**, 063103.
58 S.-D. Guo, W.-Q. Mu, J.-H. Wang, Y.-X. Yang, B. Wang and Y.-S. Ang, *Phys. Rev. B*, 2022, **106**, 064416.
59 P. Liu, G. Zhang, Y. Yan, G. Jia, C. Liu, B. Wang and H. Yin, *Appl. Phys. Lett.*, 2021, **119**, 102403.
60 G. Kresse and J. Furthmüller, *Phys. Rev. B: Condens. Matter Mater. Phys.*, 1996, **54**, 11169–11186.
61 P. E. Blöchl, *Phys. Rev. B: Condens. Matter Mater. Phys.*, 1994, **50**, 17953–17979.
62 J. P. Perdew, K. Burke and M. Ernzerhof, *Phys. Rev. Lett.*, 1996, **77**, 3865–3868.
63 Y. Zhu, X. Wang and W. Mi, *J. Mater. Chem. C*, 2019, **7**, 2049–2058.
64 E. J. Telford, A. H. Dismukes, R. L. Dudley, R. A. Wiscons, K. Lee, D. G. Chica, M. E. Ziebel, M. G. Han, J. Yu, S. Shabani, A. Scheie, K. Watanabe, T. Taniguchi, D. Xiao, Y. Zhu, A. N. Pasupathy, C. Nuckolls, X. Zhu, C. R. Dean and X. Roy, *Nat. Mater.*, 2022, **21**, 754–760.
65 F. Xue, Y. Hou, Z. Wang and R. Wu, *Phys. Rev. B*, 2019, **100**, 224429.
66 B. Wang, Y. Zhang, L. Ma, Q. Wu, Y. Guo, X. Zhang and J. Wang, *Nanoscale*, 2019, **11**, 4204–4209.
67 H. Xiang, E. Kan, S.-H. Wei, M.-H. Whangbo and X. Gong, *Phys. Rev. B: Condens. Matter Mater. Phys.*, 2011, **84**, 224429.